Impact of Dual Variable Speed and Inlet Valve Control on the Efficiency and Operating Range of Low-Head Contra-Rotating Pump-Turbines

Citation for the original published paper (version of record):
Truijen, D., Hoffstaedt, J., Fahlbeck, J. et al (2024). Impact of Dual Variable Speed and Inlet Valve Control on the Efficiency and Operating Range of
Low-Head Contra-Rotating Pump-Turbines. IEEE Access, 12: 86854-86868.
http://dx.doi.org/10.1109/ACCESS.2024.3416679

IEEE Access
Multidisciplinary | Rapid Review | Open Access Journal

Received 3 May 2024, accepted 15 June 2024, date of publication 19 June 2024, date of current version 27 June 2024.

Digital Object Identifier 10.1109/ACCESS.2024.3416679

RESEARCH ARTICLE

Impact of Dual Variable Speed and Inlet Valve Control on the Efficiency and Operating Range of Low-Head Contra-Rotating Pump-Turbines

DAAN P. K. TRUIJEN[1,2], (Graduate Student Member, IEEE), JUSTUS P. HOFFSTAEDT[3], JONATHAN FAHLBECK[4], ANTONIO JARQUIN LAGUNA[3], HÅKAN NILSSON[4], KURT STOCKMAN[1,2], AND JEROEN D. M. DE KOONING[1,2], (Senior Member, IEEE)

[1]Department of Electromechanical, Systems and Metal Engineering, Ghent University, 8500 Kortrijk, Belgium
[2]FlandersMake@UGent—Corelab MIRO, Flanders Make, Belgium
[3]Department of Maritime and Transport Technology, Delft University of Technology, 2628 CD Delft, The Netherlands
[4]Department of Mechanics and Maritime Sciences, Chalmers University of Technology, 412 96 Gothenburg, Sweden

Corresponding author: Daan P. K. Truijen (daan.truijen@ugent.be)

This work was supported by the European Union's Horizon 2020 Research and Innovation Programme under Grant 883553, and in part by the Swedish Research Council under Grant 2022-06725 and Grant 2018-05973.

ABSTRACT In an effort to make pumped hydropower storage (PHS) technology feasible for regions with a flat topography, recent research shows promising results using a contra-rotating reversible pump-turbine at low-head. In this study, the impact of dual variable speed and inlet valve control is analyzed to evaluate the effect of these three degrees of freedom (DOFs) on the system efficiency and operating range. To this end, analytical models are described to assess pump-turbine performance, conduit losses and electromechanical losses. Methodologically, optimal efficiency maps are computed for every combination of the three DOFs to evaluate individual and combined effects on the overall efficiency. Furthermore, three energy storage cycles are analyzed to further study the performance in realistic use-cases. Key conclusions include an increase in round-trip efficiency by combining variable speed ratio and inlet valve control of 5.6% and 2.0% compared with only variable speed ratio control and variable inlet valve control, respectively. Furthermore, it is shown that using only 1 DOF significantly limits the operating range, with the addition of a variable inlet valve granting a higher impact than a variable speed ratio. Combining inlet valve and speed ratio control leads not only to the highest efficiency, but also the largest operating range, with a maximum round-trip efficiency of 67.5% and an energy storage capacity of 58.6 Wh/m^2. The results confirm that exploiting both dual variable speed operation and inlet valve control yields the maximum efficiency and operating range, and is thus the preferred topology for contra-rotating reversible pump-turbines in low-head operation.

INDEX TERMS Hydropower storage, energy efficiency, MIMO system, dual rotor pump-turbine, cycle efficiency.

I. INTRODUCTION

Throughout the last decade, the global implementation of renewable energy sources has increased rapidly, with their share of global power generation having increased from below 20% in 2010 to 30% in 2022 [1]. Wind energy and photovoltaic (PV) technologies have seen the steepest rise, going from an installed capacity share of respectively 3.5% and 0.8% in 2010 to respectively 10.8% and 12.8% in 2022. By 2027, the share of wind energy is predicted to reach 14.4%, with the share of solar PV expected to increase to 22.2%, becoming the largest installed

The associate editor coordinating the review of this manuscript and approving it for publication was Alfeu J. Sguarezi Filho.

electricity capacity worldwide over hydropower, natural gas and coal [2]. As the penetration of these intermittent and non-dispatchable energy sources increases and partially replaces traditional high-inertia and dispatchable energy sources, energy storage systems are indispensable to preserve the reliability and stability of the power system. Among the different energy storage systems installed today, pumped hydropower storage (PHS) has the lowest cost [3] and accounts for more than 90% of global installed energy storage capacity [4]. High-head PHS systems exhibit a considerable lifetime and round-trip efficiencies between 70% and 85% [5]. Next to compensating for seasonal and hourly fluctuations, dynamic storage systems are necessary to support the grid frequency on a timescale of minutes to seconds through frequency restoration reserve (FRR) or frequency containment reserve (FCR). For this purpose, recent investments in hydrogen storage and electrochemical battery storage (including lead-acid, sodium-sulfur, and lithium-ion) have seen a significant increase. However, they both have significantly lower lifetimes (respectively 10-20 years and 5-15 years) compared with PHS, with their efficiencies ranging from 20% to 66% for hydrogen storage and 70% to 90% for batteries [5]. Although PHS is mostly seen as a bulk-type energy storage for hourly to seasonal storage and as frequency restoration reserve due to its high capacity, over 90% of all FCR was performed by hydropower systems during the frequency containment project in the Nordic regional group [6]. Although FCR requirements have evolved in terms of response time and stability, new variable speed PHS systems can be employed for FCR [7].

Traditionally, PHS has been limited to mountainous regions, due to the typical radial and mixed-flow pump-turbines (most commonly Francis turbines) reaching a high efficiency at a high fallhead and a low flow rate. Employing these machines at low-head would either significantly reduce the power if the flow rate is decreased accordingly, or reduce the efficiency if a higher flow rate is used [8]. Furthermore, as the conduit losses scale quadratically with flow velocity, short conduit lengths and high diameters are necessary to retain a high system efficiency, limiting the maximum distance between the two reservoirs. Therefore, the possibility of integrating low-head PHS in a ring dam in the North Sea has been discussed in [9] and [10]. The main drawback is the large investment cost associated with the ring dam. However, the added benefit that is provided by integrating this energy storage installation with existing offshore wind farms or undersea grid interconnections is promising, as has been extensively described in literature for onshore PHS integration with wind and PV farms [11], [12]. Another undismissable constraint on PHS installations is the ecological and environmental impact. Previously, it was shown that hydropower installations using suitable fish screens and fish passages are fish-friendly regarding mortality and physical injury [13]. Specifically for fish species in the North Sea, the hormonal stress levels for fish in various flow velocities was analyzed by measuring cortisol concentrations, showing that flow velocities greater than 0.2 m/s should be avoided [14].

Recently, a novel axial contra-rotating (CR) reversible pump-turbine (RPT) was presented in [15]. This RPT comprises two runners with opposite rotational motion, which reduces swirl development and increases efficiency in a low-head-high-flow system [16]. Although this dual rotor CR RPT concept is promising, the question arises as to which degrees of freedom (DOF) should be used in the control architecture to maximize the round-trip efficiency and operating range under variable operating conditions. As this CR RPT is applied in a low-head PHS system supporting the grid, both the fallhead and power setpoints are variable in time. In recent literatures [17] and [18] investigated how variable speed and variable guide vane operation of a Francis RPT increases the efficiency at off-design operation. However, the analysis only includes turbine mode and is limited to the high-efficiency region. No conduit losses or electromechanical losses are considered. In [19], it is described how variable speed operation of a low-head single rotor pump-as-turbine (PAT) allows to reach an optimal efficiency for varying fallhead in both pump and turbine mode, with a reported round-trip efficiency of 42%. Although the RPT and electric machine efficiencies were included in the efficiency analysis, the hydraulic conduit losses were not. Furthermore, the inlet valve was not considered during continuous operation. In [20], it was shown how using the blade angle and guide vane direction of a single rotor Deriaz type pump-turbine as variable DOFs can extend the operating range and increase efficiency. However, variable rotational speed was not analyzed and the conduit losses and electric machine losses were excluded from the analysis. Next, the application of dual rotor contra-rotating turbomachinery for energy generation has been described in [21] and [22], where the impact of the two rotors' speeds at different speed ratios on the efficiency is described. However, the contra-rotating machine is only described in turbine mode at a constant fallhead and no inlet valve is considered. Finally, the operation and revenue of a contra-rotating pump-turbine at variable head and variable speed has been described in [9]. However, the effect of a variable speed ratio or inlet valve was not analyzed and electromechanical losses were not included.

Therefore, the aim and originality of this paper are to analyze the full system efficiency of a PHS system using the novel CR RPT for varying fallhead and power setpoints. Furthermore, three control DOFs are considered to maximize the system efficiency over its full operating range: the first RPT runner's speed, the second runner's speed, and a controllable inlet valve angle. This inlet valve is an imperative part of the system in start-stop scenarios [23], but can also be used in continuous operation. To quantify the benefit in terms of efficiency by using all three DOFs, the analysis is repeated for all possible combinations and the results are compared. The novelty of this paper is twofold:

- First, the evaluation of the full system efficiency, including hydraulic, mechanical, and electrical efficiency, of a low-head PHS system using a CR RPT has not been described in literature.
- Furthermore, the quantification of the impact of using all available DOFs on the system efficiency and operating range is of general interest for other PHS systems that aim to extend their current capabilities. This analysis is performed over the system's full operating range, i.e., for varying fallhead and power.

In this paper, analytical models for the different system components are described in Section II. Section III describes the methodology of the paper. Here, it is explained how the full system model is used to find the optimal combination of the available DOFs to achieve an optimal efficiency at a certain fallhead and power setpoint. Furthermore, three realistic storage cycles are defined, comprising an optimal efficiency cycle, an FCR cycle, and an FFR cycle. In Section IV, the research results are outlined. Section IV-A first shows the optimal efficiency that can be reached using both variable speed ratio and inlet valve control, and it is analyzed how the optimal speed ratio and inlet valve angle vary over the operating range. Next, it is described how the optimal efficiency and operating range change when variable speed ratio control and/or variable inlet valve control is omitted. In Section IV-B, the different cycle efficiencies and energy capacities are described, while retaining focus on the impact of the different DOFs. Finally, the quantitative results are discussed in Section V.

II. SYSTEM MODELING

To simulate the different control approaches, all system components are modeled to accurately reflect the steady-state losses in the system. In this analysis, the generator reference system is used, i.e., the flow rate Q, the runner rotational speeds $\omega_{1,2}$ and the power P are positive in turbine (generator) mode. However, when operation in pump mode is described throughout the text, an increase of a value refers to the magnitude of that value, i.e., a power of -8 MW is higher than -7 MW. All simulations in this paper are performed using MATLAB® & Simulink® R2022b.

A. HYDRAULIC MODEL

The hydraulic model comprises the contra-rotating RPT model and the conduit model, which includes the inlet valve. A schematic overview of the full system is shown in Fig. 1. The CR RPT, described in [15], has a nominal power of 10 MW at a maximum fallhead of 10 m and is designed to have an efficiency $>$ 90% in both pump and turbine mode. The design speed ratio is $\zeta_d = \omega_2/\omega_1 = 0.9$. The RPT characterization is based on a range of 180 steady-state computational fluid dynamics (CFD) simulations. The CFD simulations are performed using the foam-extend revision 2d9985 (4.1 nextRelease) open source CFD code. Turbulence is modeled using the k-ω SST (shear stress transport)

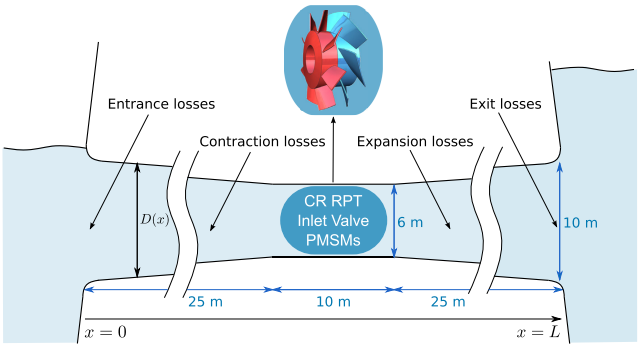

FIGURE 1. Schematic overview of the system with indicated conduit dimensions and minor losses (for flow in pump mode).

two equation eddy-viscosity model. The numerical domain consists of one blade passage per runner with a total of $1.4 \cdot 10^6$ cells. To emulate the full runners, cyclic boundaries and a mixing-plane between the runners are used. The runner rotation is modeled using the MRF approach. To characterize the runners with the results of the CFD computations, the pressure heads $h_{1,2}$ of the runners are adimensionalized by dividing with the dynamic head (1). The resulting pressure head coefficients $C_{h1,2}$ as well as the efficiencies $\eta_{h1,2}$ are a function of both tip speed ratios (TSR) $\lambda_{1,2}$. The TSRs are defined as the tangential velocity of the runner tips $R\,\omega_{1,2}$ divided by the average flow velocity Q/A (2). Here, R and A are the runner radius and area, respectively.

$$C_{h1,2} = \frac{g\,h_{1,2}}{\frac{1}{2}(Q/A)^2} \tag{1}$$

$$\lambda_{1,2} = \frac{R\,\omega_{1,2}}{Q/A} \tag{2}$$

Figure 2 shows the characteristic curves for $C_{h1,2}$ and $\eta_{h1,2}$ in both pump and turbine mode, with each line representing different speed ratios ζ. As the RPT characteristics are highly non-linear, 2D-lookup tables with linear interpolation are used to define $C_{h1,2}$ and $\eta_{h1,2}$. These are based on the aforementioned steady-state CFD simulations. The stability limits for the TSRs are $0.3 < \lambda_1 < 3.6$ and $2.7 < \lambda_1 < 8$ in turbine and pump mode respectively. The variability of the speed ratio in this analysis is $0.8 \leq \zeta \leq 1.0$. Finally, the hydraulic torque $\tau_{h1,2}$ is calculated using (3) in turbine mode. In pump mode, $\eta_{h1,2}$ is placed in the denominator instead of the nominator.

$$\tau_{h1,2} = \frac{\rho\,g\,Q\,h_{1,2}\,\eta_{h1,2}}{\omega_{1,2}} \quad \text{(Turbine)} \tag{3}$$

The conduit in this system is symmetrical and has a total length of 60 m (see Fig. 1). The RPT is centered in a 10 m long section with a diameter of 6 m. Towards the two reservoirs, the diameter is linearly increased to a diameter of 10 m with a cone length of 25 m. The losses that occur in the conduit can be divided into the major and minor losses. The major losses occur due to friction within the conduit and are calculated

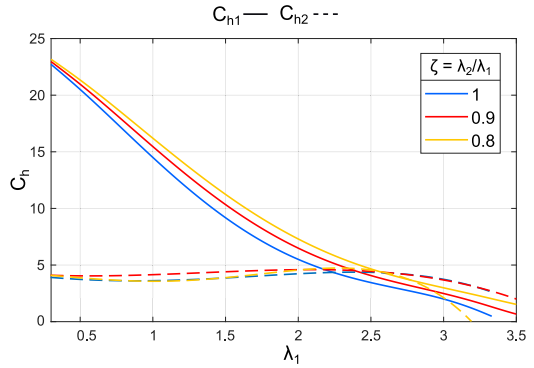

(a) Head coefficients in turbine mode.

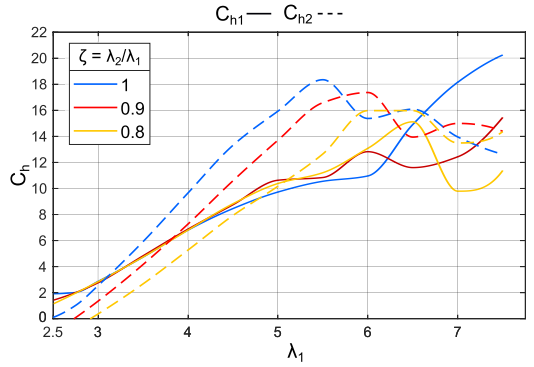

(b) Head coefficients in pump mode.

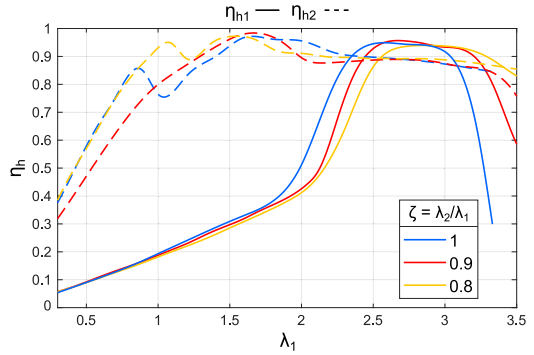

(c) Efficiency in turbine mode.

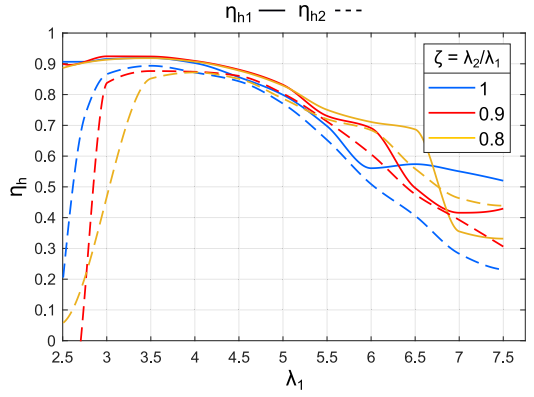

(d) Efficiency in pump mode.

FIGURE 2. RPT's head coefficients $C_{h1,2}$ and efficiency $\eta_{h1,2}$ versus TSRs $\lambda_{1,2}$ for different speed ratios ζ.

using (4), better known as the Darcy-Weisbach formula:

$$h_{L,M} = \int_0^L f(x)\frac{1}{D(x)}\frac{v^2(x)}{2g}\,dx\,, \tag{4}$$

TABLE 1. Conduit parameters used for the simulations.

Conduit dimensions		
Conduit length	L [m]	60
Conduit outer diameter	D_o [m]	10
Conduit RPT diameter	D_{RPT} [m]	6
Relative roughness	e [mm]	3
Minor loss coefficients		
Entrance	[-]	0.05
Exit	[-]	1
Expansion	[-]	0.04
Contraction	[-]	0.13
Inlet valve	k_v [-]	variable

$$\text{where } v(x) = \frac{4\cdot Q}{\pi\cdot D^2(x)} \tag{5}$$

Here, x is the horizontal distance from the left reservoir entrance, L is the total conduit length, $D(x)$ is the diameter of the conduit and g is the gravity constant. $f(x)$ is the friction factor and is approximated by the Colebrook-White equation for turbulent flow, where e is the relative roughness, listed in Table 1:

$$\frac{1}{\sqrt{f(x)}} = -2\log\left(\frac{e}{3.7\cdot D(x)}\right) \tag{6}$$

The minor losses include all local flow losses (indicated in Fig. 1) and are calculated as follows:

$$h_{L,m} = \sum_i k_i\frac{v_i^2}{2g} = \sum_i k_i\frac{8}{\pi^2 D_i^4}\frac{Q^2}{g} \tag{7}$$

In this equation, k_i are the minor loss coefficients, listed in Table 1. Note that the inlet valve has a variable loss coefficient k_v, which is inversely proportional to its opening state. Varying k_v influences the conduit losses and can thus be used as a DOF. The relation between k_v and the valve opening state can be found in the manufacturer's datasheets. However, in this paper, the results are given as a function of k_v to allow general conclusions to be drawn, regardless of the inlet valve type.

B. ELECTROMECHANICAL MODEL

The electromechanical model consists of the electric machines, the power electronics, and the mechanical drivetrain. For the electric machines, permanent magnet synchronous machines (PMSM) are used and are modeled in the rotating dq reference frame, where the stator copper losses and iron losses are represented by resistances R_s and R_c. The value of R_c depends on the rotational speed and is given by (8), where K_f and K_h are constants representing eddy current losses and hysteresis losses, respectively [24].

$$R_c = \frac{1}{K_f + K_h/\Omega} \tag{8}$$

The PMSM parameters are listed in Table 2. The two machines are designed to match their respective RPT runners with the methods described in [25]. Fig. 3a and Fig. 3b respectively show the efficiency maps for PMSM 1 and PMSM 2. Here, the machines are controlled using field

TABLE 2. PMSM parameters in the *dq* reference frame.

		PMSM 1	PMSM 2
Nominal speed	ω_{nom} [rad/s]	4.8	4.8
Nominal torque	τ_{nom} [10^5·Nm]	9.93	14.7
# pole pairs	p [-]	63	63
Flux linkage	Ψ [Wb]	9.45	9.45
Stator resistance	R_{s} [mΩ]	51.4	34.7
Inductance	$L_{\text{d}}, L_{\text{q}}$ [μH]	456	308
Eddy current factor	K_{f} [mS]	3	3
Hysteresis factor	K_{h} [mS/s]	300	300

TABLE 3. Variable frequency drive (IGBT) parameters [30] and drivetrain friction torque coefficients.

DC-bus voltage	V_{DC} [V]	3300
Collector-emitter voltage drop	$V_{\text{CE},0}$ [V]	3.8
Forward resistance	R_{f} [μΩ]	85
Switch on energy	E_{on} [J]	1.89
Switch off energy	E_{off} [J]	1.95
Reference current	i_{ref} [A]	1200
Friction torque coefficient	F_1 [Nm·s]	4138
Friction torque coefficient	F_2 [Nm·s]	6125

oriented control (FOC). With FOC, the i_{d} current is regulated to 0. As a result, the torque is directly proportional to i_{q}, simultaneously allowing the generator efficiency η_{g} and the motor efficiency η_{m} to be calculated as in (9), where τ_{m} is the PMSM torque.

$$\eta_{\text{g}} = \frac{\frac{3}{2}\, v_{\text{q}}\, i_{\text{q}}}{\omega\, \tau_{\text{m}}}, \quad \eta_{\text{m}} = \frac{\omega\, \tau_{\text{m}}}{\frac{3}{2}\, v_{\text{q}}\, i_{\text{q}}} \tag{9}$$

Note that the efficiency in motor mode is slightly higher at the nominal operating point, with a less severe efficiency decrease towards the high-speed-low-torque and low-speed-high-torque zones. The peak electromechanical efficiency of 97.2% corresponds to the state-of-the-art Axial Flux PMSMs described in literatures [26] and [27].

Next, the variable frequency drives (VFDs) are modeled. In commercially available medium voltage VFDs with an active front end, three-level neutral point clamped inverters with high voltage IGBTs are commonly applied. Among others, Danfoss Vacon® 3000 and TMEIC TMdrive®-50 report nominal efficiencies η_{VFD} of 98.8%, 98.5% respectively [28], [29]. However, no supplier provides information on how the efficiency evolves along the operating range. Therefore, a simplified loss model is constructed with parameters from a medium voltage IGBT [30]. The main losses of a VFD are the conduction losses P_{con} and the switching losses P_{sw} [31], which can be calculated for each IGBT as follows:

$$P_{\text{con}} = f_{\text{out}} \int_0^{1/f_{\text{out}}} \left[V_{\text{CE},0} \cdot i(t) + R_{\text{f}} \cdot i^2(t)\right] dt \tag{10}$$

$$P_{\text{sw}} = f_{\text{out}} \left(\sum_j \frac{E_{\text{on}}}{i_{\text{ref}}}\, i(j) + \sum_y \frac{E_{\text{off}}}{i_{\text{ref}}}\, i(y) \right) \tag{11}$$

Here, f_{out} is the output frequency, $V_{\text{CE},0}$ is the collector-emitter voltage drop, R_{f} is the forward resistance, E_{on} and E_{off} are the switching energy losses, specified in the datasheet, and i_{ref} is the reference current at which these energy measurements were performed by the manufacturer. j and y are vectors that contain the times at which the switches respectively open and close in one fundamental period. To determine these, a variable frequency sinusoidal voltage is generated with pulse width modulation using two symmetrical level-shifted triangle carriers with a carrier frequency of $f_{\text{sw}} = 1$ kHz, which is also used by the aforementioned manufacturers. The used parameters are listed in Table 3. The full efficiency map of the VFD is pictured in Fig. 3c. Note that the smaller losses, such as the DC-bus losses have been excluded in this simplified model because they are mostly negligible compared with the aforementioned losses.

Finally, the electromechanical model is connected to the hydraulic model through the drivetrain in (12), which relates the angular velocities $w_{1,2}$ to the hydraulic torque $\tau_{h1,2}$ and the machine torque $\tau_{m1,2}$. In this analysis, the bearing friction is modeled through a simplified constant friction torque coefficient $F_{1,2}$, found in Table 3, which results in a 2% power loss at the nominal operating point [32].

$$\tau_{\text{h1,2}} = \tau_{\text{m1,2}} + F_{1,2}\, \omega_{1,2} \tag{12}$$

III. METHODOLOGY

A. OPTIMAL EFFICIENCY DATASET

Using the system models outlined in Section II, a numerical dataset $\mathcal{D} : \mathbb{R}^4 \rightarrow \mathbb{R}^3$ is calculated. The dataset $\mathcal{D}$ relates four input variables, i.e. the three varying DOFs ω_1, ω_2, k_{v} and the fallhead Δh, to three crucial output parameters, i.e. the flow rate Q, electrical power P_{e} and total efficiency η_{tot}:

$$\mathcal{D}(\omega_1, \omega_2, k_{\text{v}}, \Delta h) = [Q, P_{\text{e}}, \eta_{\text{tot}}] \tag{13}$$

The dataset $\mathcal{D}$ is populated by numerically varying the inputs over the following intervals:

$$\omega_1 \in [-4.8 : 0.1 : 4.8] \text{ in rad/s} \tag{14}$$

$$\omega_2 \in [-4.8 : 0.1 : 4.8] \text{ in rad/s} \tag{15}$$

$$k_{\text{v}} \in [0 : 0.5 : 50] \tag{16}$$

$$\Delta h \in [1 : 0.5 : 10] \text{ in m} \tag{17}$$

Here, the standard MATLAB® vector notation is used, including the data increments for each variable, which determine the resulting resolution of the dataset $\mathcal{D}$.

For each combination of input variables, the flow rate Q is calculated by applying the law of conservation of energy for a steady and incompressible flow (18):

$$h_1(Q) + h_2(Q) + \text{sign}(Q) \cdot h_{\text{L}}(Q) = \Delta h \tag{18}$$

In this equation, $h_{1,2}$ are the RPT runner heads (1) and h_{L} is the sum of the major and minor losses (4) and (7). This equation is numerically solved for the full range of ω_1, ω_2, k_{v} and Δh, using the lookup tables for $C_{\text{h1,2}}$. Next, the machine torques are calculated by combining (1), (3) and (12), again using the lookup tables for $C_{\text{h1,2}}$ and $\eta_{\text{h1,2}}$:

$$\tau_{\text{m1,2}} = \frac{\rho\, g\, Q\, h_{1,2}\, \eta_{\text{h1,2}}}{\omega_{1,2}} - F_{1,2}\, \omega_{1,2} \tag{19}$$

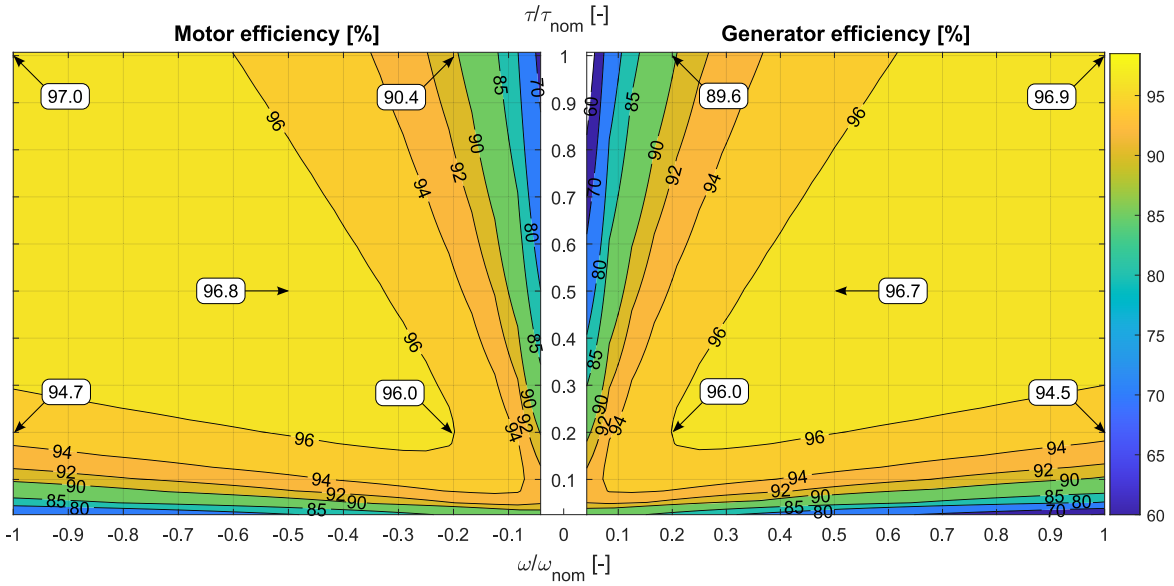

(a) PMSM 1 efficiency

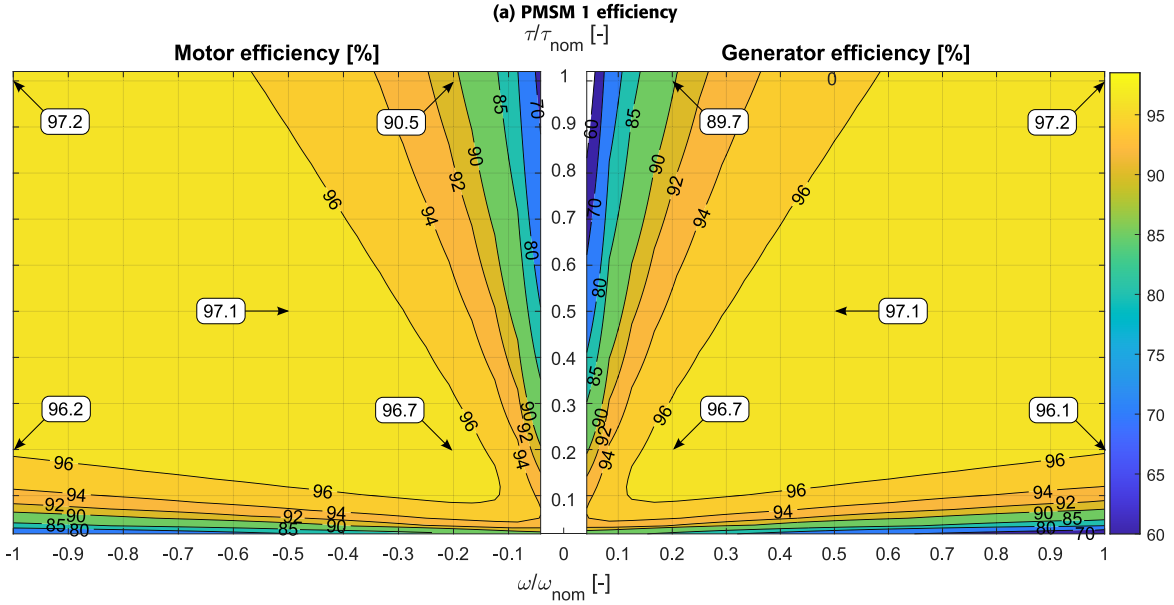

(b) PMSM 2 efficiency

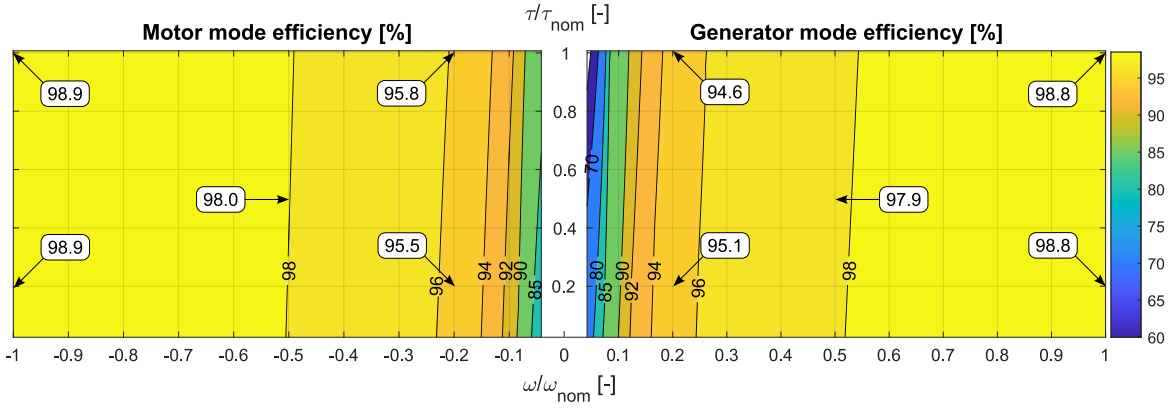

(c) VFD efficiency

FIGURE 3. Efficiency map of (a) PMSM 1, (b) PMSM 2 and (c) the variable frequency drive plotted versus normalized speed and torque.

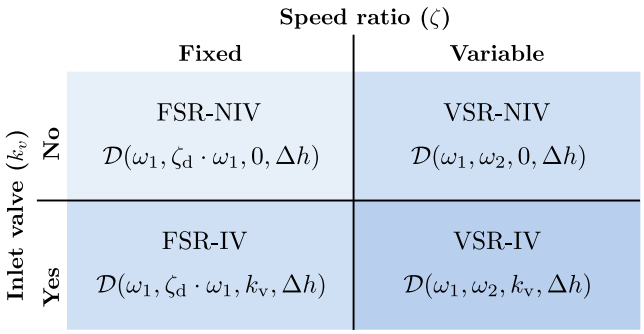

FIGURE 4. Overview of the different topologies, i.e., combinations of DOFs in the control architecture.

Finally, the electrical power is calculated using the efficiency maps for the PMSMs and VFD, with (20) used in turbine mode. The total efficiency in turbine mode is found using (21).

$$P_e = \omega_1 \, \tau_{m1} \, \eta_{g1} \, \eta_{g,VFD} + \omega_2 \, \tau_{m2} \, \eta_{g2} \, \eta_{g,VFD} \tag{20}$$

$$\eta_{tot} = \frac{P_e}{\rho \, g \, Q \, \Delta h} \quad \text{(Turbine)} \tag{21}$$

The four possible DOF combinations are denoted 'topologies' and are listed in Fig. 4. In a system with a fixed speed ratio and no inlet valve control (FSR-NIV), only one DOF is used, being the first runner's speed. The second runner's speed is controlled to always be at the design speed ratio $\zeta_d = 0.9$ to the first runner and the inlet valve is not used during continuous operation ($k_v = 0$). Therefore, the FSR-NIV topology corresponds to the reduced dataset $\mathcal{D}(\omega_1, \zeta_d \cdot \omega_1, 0, \Delta h)$. In topology VSR-NIV, the speed ratio is variable and the second runner's speed is thus added as a DOF, corresponding to the dataset $\mathcal{D}(\omega_1, \omega_2, 0, \Delta h)$. Next, topology FSR-IV adds the inlet valve as a DOF, while maintaining a fixed speed ratio: $\mathcal{D}(\omega_1, \zeta_d \cdot \omega_1, k_v, \Delta h)$. Finally, in a system with VSR-IV, all three DOFs are used, and the complete generated dataset $\mathcal{D}$ is used to analyze this topology.

To be able to evaluate the different DOF combinations, an efficiency map is created for each topology that reflects the maximum efficiency at each fallhead Δh and power setpoint $P_e \in [-10 : 0.5 : 10]$ MW across the operating range. Using the power maps, all combinations of the DOFs that satisfy the power setpoint at a certain fallhead, can be found using 1D, 2D or 3D interpolation depending on the number of DOFs. With the interpolated parameters, the efficiency is recalculated. For every DOF combination, the combination of parameters that reaches the highest efficiency is saved together with this efficiency in lookup tables.

B. CYCLE EFFICIENCY

Finally, three full energy storage cycles are analyzed. The cycles are defined to store electrical energy in pump mode until the maximum possible fallhead is reached and then switch to turbine mode until the lowest possible fallhead is reached. The change in fallhead is calculated using (22), where A_r is the reservoir area.

$$\frac{d[\Delta h(t)]}{dt} = 2\frac{Q(t)}{A_r} \tag{22}$$

During both pump and turbine mode, both the hydraulic energy E_h and electrical energy E_e are monitored, which allows to calculate the cycle pumping efficiency $\eta_p = E_h/E_{e,p}$, the cycle turbining efficiency $\eta_t = E_{e,t}/E_h$ and the full cycle (or round-trip) efficiency $\eta = E_{e,t}/E_{e,p} = \eta_t \cdot \eta_p$. Although a reservoir area of $A_r = 1 \cdot 10^6$ m^2 is used for all simulations, the results of E_h are reported per unit reservoir area Wh/m^2 to generalize the conclusions. Note that tidal head variations are not included in this analysis to keep the results general.

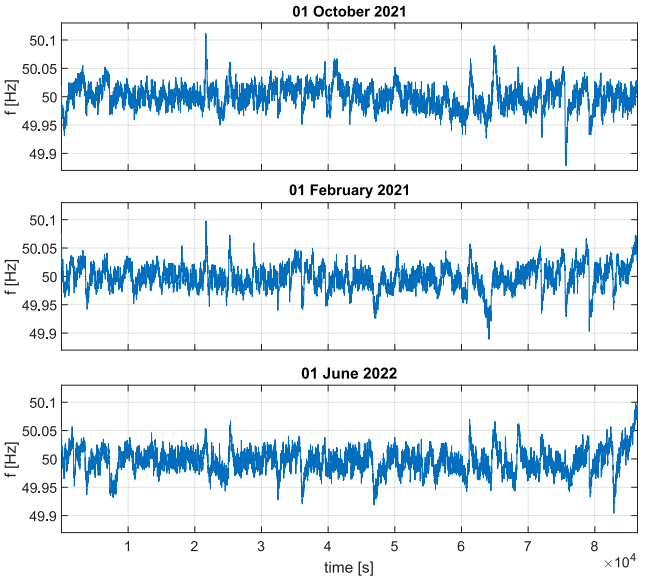

FIGURE 5. Measured grid frequency in Germany for the first days of October 2021, February 2022 and June 2022 [33].

Cycle I is performed at a variable power at optimal efficiency to represent the system round-trip efficiency. Throughout the cycle, the power setpoint is chosen that results in the highest efficiency at the current fallhead.

Cycle II represents a cycle in which the system participates in frequency containment reserve (FCR) with a reserve capacity of $P_r = 1$ MW on top of a baseline power P_b. Here, the reserve capacity is partially or fully activated based on the actual grid frequency $f(t)$. If the frequency deviation $\Delta f = f(t) - 50$ Hz is smaller than 10 mHz, no reserve power is delivered and the system operates at the baseline power. Outside this deadband, the delivered reserve scales linearly up to a frequency deviation of $|\Delta f| = 200$ mHz:

$$P(t) = P_b(t) + \frac{50\text{Hz} - f(t)}{0.19\text{Hz}} \cdot P_r \tag{23}$$

When $|\Delta f| > 200$ mHz, the full capacity of either $P_b(t) + P_r$ or $P_b(t) - P_r$ is activated. To not be influenced by the characteristic frequency patterns of one particular day or

season, the FCR cycle is run for three randomly selected historic frequency datasets in Germany with a sample time of 1 s, archived by TransnetBW [33]. Fig. 5 shows the three datasets used, which are the measured frequencies for the first day of respectively October 2021, February 2022 and June 2022.

Cycle III represents a frequency restoration reserve (FRR) scenario where a certain constant power setpoint must be maintained for a longer time period. In this cycle, the power in pump mode is kept constant at -10 MW until the highest possible fallhead and the power in pump mode is kept constant at 1 MW until the lowest possible fallhead is achieved.

IV. RESULTS

A. OPTIMAL EFFICIENCY MAPS

In this subsection, topology VSR-IV, which uses all three DOFs, is used as a baseline, with the efficiency maps of the other topologies compared with topology VSR-IV.

1) TOPOLOGY VSR-IV

Fig. 6a shows the maximum overall system efficiency for every power setpoint P and measured fallhead Δh. In turbine mode, a power of 10 MW can be generated down to a fallhead of 9 m, with a power of 1 MW possible for fallheads down to 2 m. The maximum efficiency for each fallhead is reached close to the maximum power that can be generated from that fallhead, i.e., the operating range limit, with an overall maximal efficiency of 82.9%. The efficiency decreases towards the high-head-low-power zones, which is where the inlet valve coefficient k_v is the highest (Fig. 6b). Note that, except at the operating range limit, k_v is always greater than 0. This means that at all operating points that have 'excess' head to produce the wanted power, it is more efficient to reduce the conduit efficiency by closing the valve to increase the overall efficiency. This phenomenon is caused by the RPT characteristics shown in Fig. 2a and 2c. For each fallhead, the sum of the turbine heads $h_{1,2}$ and the conduit head loss h_L must match this fallhead (18). To generate a high head, the runners' TSRs must decrease, simultaneously significantly reducing their efficiency. Therefore, increasing h_L with the inlet valve (and thus decreasing the conduit efficiency) allows the RPT to run at their optimal TSRs and efficiency, increasing the overall efficiency. Fig. 6c pictures the turbine speed ratio at which the maximum efficiency is reached. Note that in turbine mode, the maximum efficiency is reached mostly at $0.8 < \zeta < 0.85$, with increasing speed ratio towards the operating range limits.

In pump mode, a maximum head of 9.5 m can be reached with a power of -10 MW. The maximum efficiency for each power setpoint is reached at 0.5 m to 1.5 m below the operating range limit, with an overall maximal efficiency of 84.1%. The efficiency decreases towards the low-head-high-power zones which is where, similar to turbine mode, the inlet valve is used. Note that, contrary to turbine mode, there is a large zone where the valve is fully open ($k_v = 0$). The characteristics in Fig. 2b and 2d show that for medium TSRs, $C_{h1,2}$ (and subsequently the RPT's head) is low, but the efficiency is still high, explaining why an increase of h_L with the inlet valve would only decrease the overall efficiency. However, for very low TSRs, η_{h2} experiences a steep decrease, causing the increase of k_v towards the low-head-high-power regions, shown in Fig. 6b. The optimal speed ratio in pump mode (Fig. 6c) ranges between $0.9 < \zeta < 1$, with the highest speed ratio spanning over the high-power operating points.

As previously mentioned, topology VSR-IV is used as the baseline topology. In the remainder of this section, the maximum efficiency maps of the other topologies are compared with topology VSR-IV as shown in Fig. 7.

2) TOPOLOGY FSR-IV

Fig. 7a visualizes how the maximum efficiency map changes for topology FSR-IV, in which the second runner operates at the design speed ratio of $\zeta_d = 0.9$. In turbine mode, the main difference with topology VSR-IV lies in the reduction of efficiency, with an average difference of 0.5% and a maximum of 1.7% at $\Delta h = 8.5$ m and $P = 7.5$ MW. In pump mode, the efficiency difference remains between 0.1% and 1.0% close to the operating range limit. However, in the low-head-high-power zones, this efficiency deficit increases to a maximum of 17.0% at $\Delta h = 7$ m and $P = -10$ MW. Note that this zone is where topology VSR-IV reaches its optimal efficiency with a speed ratio of $\zeta = 1$, requiring a lower inlet valve coefficient and thus increasing efficiency. Furthermore, the operating range in pump mode is decreased, as the minimum required power for a certain fallhead is higher for the design speed ratio than for the speed ratios used in topology VSR-IV. For the same power setpoints, topology FSR-IV has a head range reduction of 0.5 m for power setpoints -1.5 MW, -3.5 to -5 MW, -7 MW and -8 to -10 MW. The maximum head for this topology is 9 m, compared with 9.5 m for topology VSR-IV.

3) TOPOLOGY VSR-NIV

In Fig. 7b, the difference in efficiency and operating range compared with topology VSR-IV has increased significantly by excluding inlet valve control. In turbine mode, the operating range has decreased significantly for high fallheads as the inlet valve is no longer used to reduce net head over the turbine, leading to torque values exceeding the PMSM limit. The maximum power setpoint is reduced to 7 MW (at $\Delta h = 7$ m), with the maximum fallhead reduced to 9 m. In the remaining operating range, the efficiency also decreases compared with topology VSR-IV. For a given fallhead, the efficiency loss is 0% at the operating range limit (up to $\Delta h = 7$ m), increasing towards the lower power zones and high head zones, with a maximum efficiency deficit of 4.4% at $\Delta h = 9$ m, $P = 5.5$ MW. In pump mode, for low power setpoints, no efficiency loss exists compared to topology VSR-IV, as also in that topology, the maximum efficiency is

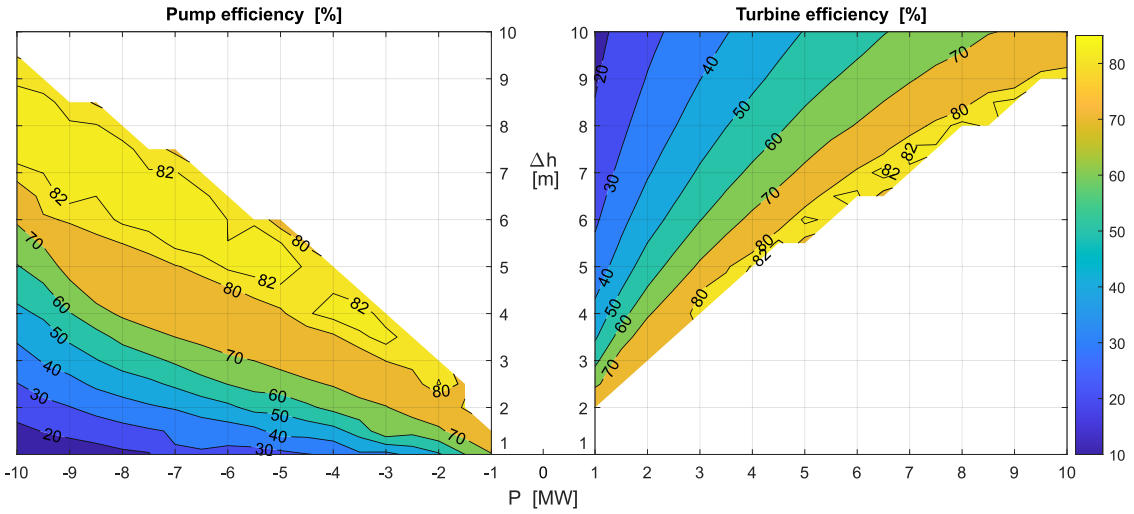

(a) Topology VSR-IV efficiency map.

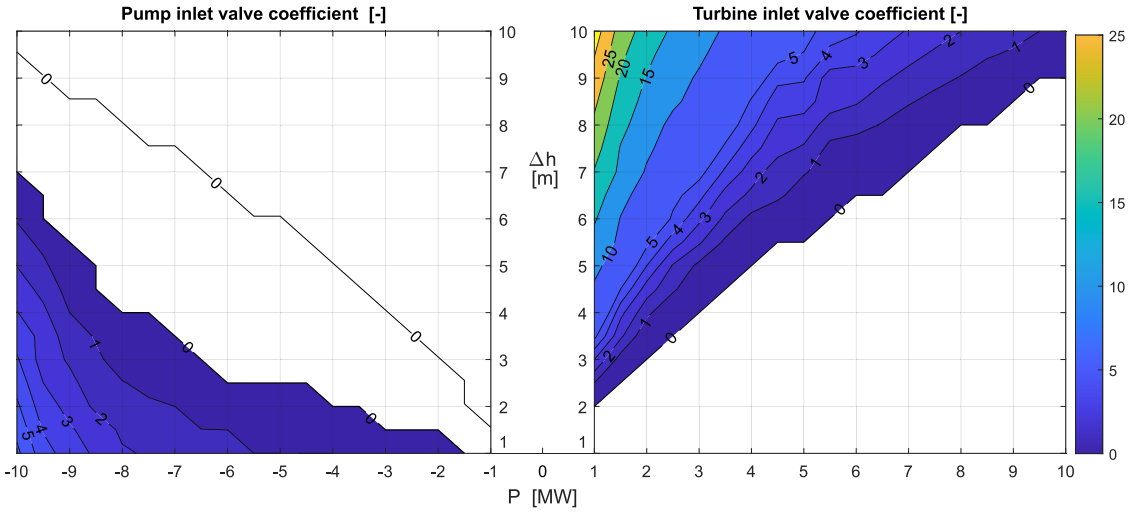

(b) Topology VSR-IV inlet valve coefficient k_v map.

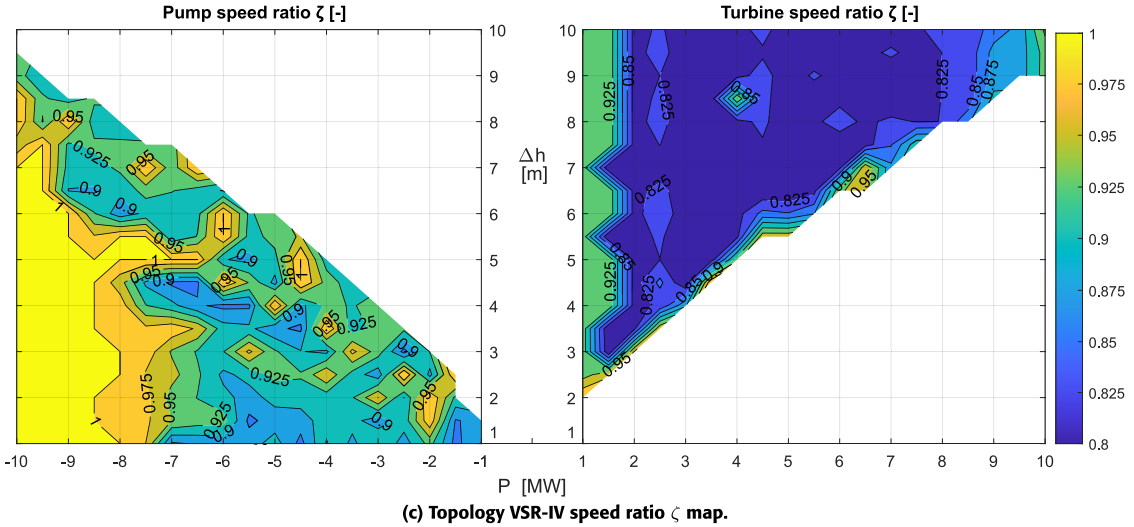

(c) Topology VSR-IV speed ratio ζ map.

FIGURE 6. (a) Efficiency, (b) inlet valve coefficient and (c) speed ratio versus power and fallhead for topology VSR-IV.

reached with a fully open inlet valve in this region (as seen in Fig. 6b). However, topology VSR-NIV cannot dissipate high powers at low fallheads without exceeding the PMSM torque limits, significantly reducing the power operating range, i.e.,

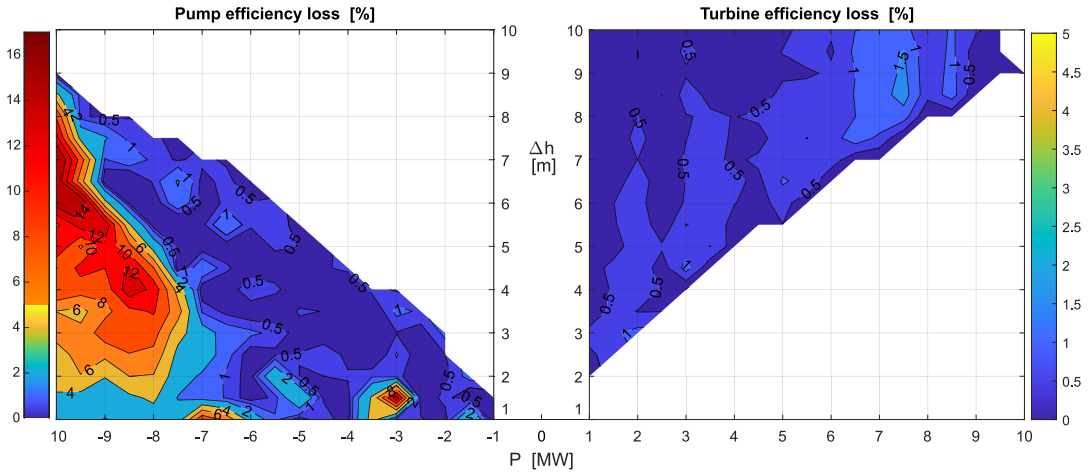

(a) Topology FSR-IV efficiency difference with topology VSR-IV.

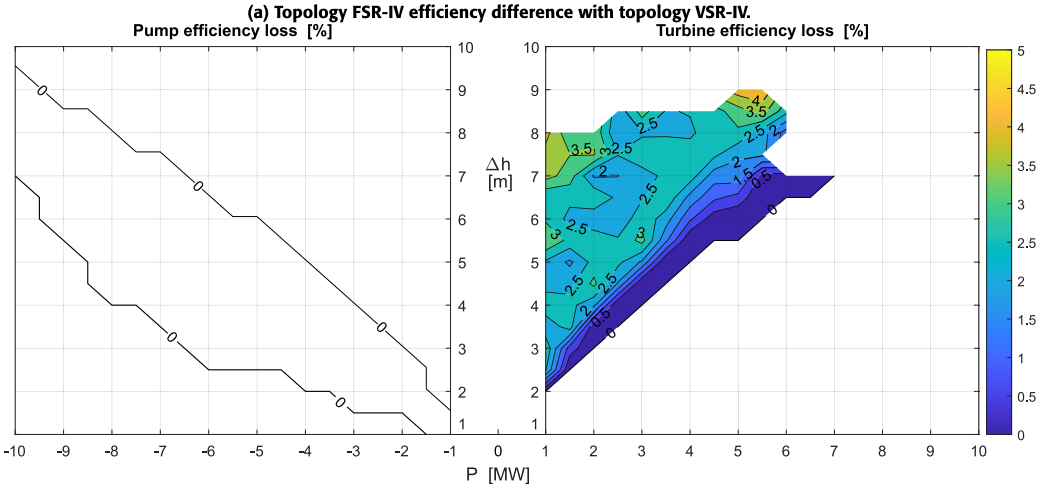

(b) Topology VSR-NIV efficiency difference with topology VSR-IV.

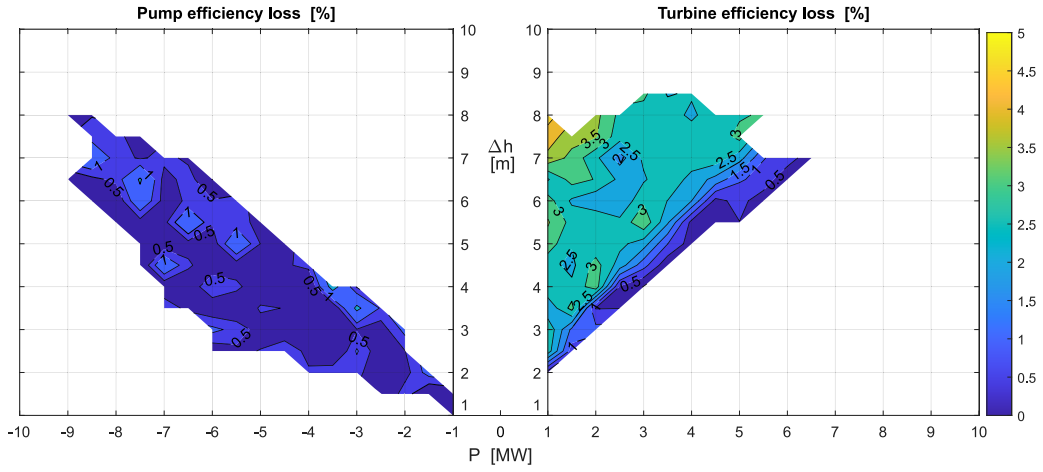

(c) Topology FSR-NIV efficiency difference with topology VSR-IV.

FIGURE 7. Efficiency difference (loss) compared with topology VSR-IV versus power P and fallhead for (a) topology FSR-IV (b) topology VSR-NIV (c) topology FSR-NIV.

the amount of power setpoints that are available at a certain fallhead.

4) TOPOLOGY FSR-NIV

In topology FSR-NIV (Fig. 7c), using the design speed ratio ζ_d and holding $k_v = 0$, the operating limits and efficiency in turbine mode are further reduced. In this topology, the maximum fallhead and power are respectively 8.5 m and 6.5 MW, with the minimum fallhead being 2 m at 1 MW. Furthermore, the efficiency reduction now ranges from 0.1% at the operating range limit for low fallheads to 4.7% for $P = 1$ MW at $\Delta h = 8$ m. In pump mode, the operating

range has reduced significantly compared with topology VSR-NIV. The maximum reachable fallhead is 8 m at a power of −9 MW, with the remaining operating range having an average reduced efficiency of 2.1%.

B. CYCLE EFFICIENCY

For the four topologies, Table 4a lists the round-trip efficiency together with the pump and turbine efficiencies separately, which result from cycle I, where the power is always chosen to result in the highest efficiency for the current fallhead Δh. Furthermore, the hydraulic energy storage capacity is outlined. The hydraulic capacity is maximal for topology VSR-IV, using three DOFs, with fallhead limits of 2 m and 9.5 m: $E_h = 58.6$ Wh/m^2. Next, the upper fallhead limit is reduced to 9 m for topologies FSR-IV (restricted by pump mode) and VSR-NIV (restricted by turbine mode). Therefore, these topologies with two DOFs have an energy capacity of $E_h = 52.4$ Wh/m^2, which is an 11% energy capacity reduction compared with topology VSR-IV. As the maximum fallhead in pump mode for topology FSR-NIV is only 8 m, its hydraulic energy capacity is reduced to $E_h = 40.8$ Wh/m^2, a 30% reduction compared with topology VSR-IV. Using all three DOFs, topology VSR-IV yields the highest cycle efficiency of 67.5%, with topology FSR-IV (excluding speed ratio control) slightly less efficient at 67.1%. Using only one DOF, topology FSR-NIV yields a reduced cycle efficiency of 64.0%. For topology VSR-NIV, the cycle efficiency of 62.7 is primarily affected by the reduced turbine efficiency towards the maximum fallhead of 9 m. From 8 m to 9 m, the maximum turbine efficiency decreases from 69.3% to 51.8%. For this topology, an alternative cycle with a lower maximum fallhead would result in a higher cycle efficiency at the cost of a lower energy capacity.

In Table 4b, the average efficiency and stored energy results of the FCR cycles with 1 MW reserves are presented. Here, the base power for each fallhead is defined as the power limit (see Fig. 6a and 7) −1 MW in turbine mode and +1 MW in pump mode. This definition of the base power allows the system to operate in its high efficiency region while ensuring that all FCR power setpoints (with a maximum reserve capacity of ±1 MW) lie within the operating range. Note that, compared with cycle I, the difference in cycle efficiency between VSR-IV (63.3%) and FSR-IV (61.3%) becomes significant. As can be seen in Fig. 7a, the efficiency difference between the two topologies is small towards the operating range limit, but increases towards the subnominal operating points. As the fluctuating FCR power setpoint forces the system to operate in these regions, the cycle efficiency for topology FSR-IV decreases further compared with VSR-IV. Furthermore, for $\Delta h > 7.5$ m, the power operating range for topology FSR-IV becomes smaller than $2 \cdot P_r = 2$ MW, resulting in a hydraulic energy capacity of 27.4 Wh/m^2. The variable speed topologies VSR-NIV and VSR-IV can operate up to $\Delta h = 8$ m, resulting in an increased energy capacity of $E_h = 32.6$ Wh/m^2. When comparing the two VSR topologies, it can be seen

TABLE 4. Cycle efficiency and electric energy capacity for three different cycles across the full possible fallhead range for the four topologies.

(a) Cycle I: Optimal efficiency cycle.

		FSR NIV	VSR NIV	FSR IV	VSR IV
Cycle efficiency	η [%]	64.0	62.7	67.1	67.5
Pump efficiency	η_p [%]	82.4	83.1	82.3	82.8
Turbine efficiency	η_t [%]	77.7	75.5	81.5	81.5
Energy capacity	E_h [Wh/m²]	40.8	52.4	52.4	58.6

(b) Cycle II: Average results of three FCR cycles with a 1 MW reserve capacity with frequency data from the first day of October 2021, February 2022, and June 2022).

		FSR NIV	VSR NIV	FSR IV	VSR IV
Cycle efficiency	η [%]	59.9	57.7	61.3	63.3
Pump efficiency	η_p [%]	81.9	82.6	82.0	82.6
Turbine efficiency	η_t [%]	73.1	69.8	74.8	76.6
Energy capacity	E_h [Wh/m²]	22.4	32.6	27.4	32.6

(c) Cycle III, reflecting FRR operation with a constant power of -10 MW in pump mode and 1 MW in turbine mode.

		FSR NIV	VSR NIV	FSR IV	VSR IV
Cycle efficiency	η [%]	–	15.7	16.3	19.2
Pump efficiency	η_p [%]	–	82.3	52.5	64.1
Turbine efficiency	η_t [%]	–	19.1	31.0	29.9
Energy capacity	E_h [Wh/m²]	–	10.2	52.4	58.6

that the pump efficiency remains identical, as the power trajectory in this FCR scenario remains within the region where the use of an inlet valve brings no increase in efficiency (Fig. 6b). However, due to the decrease in turbine efficiency for topology VSR-NIV, the cycle efficiency in this FCR scenario is only 57.7% compared with 63.3% for topology VSR-IV. Finally, the available head for the 1 DOF topology FSR-NIV further decreases in this scenario and can vary between 4 m and 7 m, again resulting in the lowest hydraulic energy capacity of 22.4 Wh/m^2. From the results, it can be seen that topology VSR-IV, using all three available DOFs, yields the highest efficiency at the highest energy capacity in this FCR scenario, with an efficiency improvement of 2.0% compared with topology FSR-IV and respectively 3.4% and 5.6% compared with topologies FSR-NIV and VSR-NIV. Furthermore, topology VSR-IV achieves a respective energy storage capacity increase of 19% and 46% compared with topologies FSR-IV and FSR-NIV.

In Table 4c, the efficiencies and hydraulic energy storage capacities are listed for cycle III, which reflects FRR operation, with constant powers of −10 MW in pump mode and 1 MW in turbine mode. As this constant power cycle forces the system to go through its low efficiency zones, the cycle efficiencies are low, with topology VSR-IV having a cycle efficiency of 19.2%, which is respectively 2.9% and 3.5% higher than topology FSR-IV and VSR-NIV. With a cycle between 2 m and 9.5 m, topology VSR-IV reaches the highest hydraulic energy storage capacity of 58.6 Wh/m^2, with the reduced maximum pump head of 9 m for topology FSR-IV resulting in a lower energy capacity $E_h = 52.4$ Wh/m^2. In the topologies without a controllable inlet valve, the operating range in pump mode at −10 MW is significantly decreased. Without a variable speed ratio,

topology FSR-NIV cannot operate at −10 MW in pump mode, whereas adding variable speed ratio, the power of −10 MW can only be reached between 7 m and 9.5 m. As the maximum fallhead at which the turbine in topology VSR-NIV can operate at 1 MW is 8 m, the hydraulic energy storage capacity for this topology is only 10.2 Wh/m^2, which is more than 5 times lower than the storage capacities of the topologies using an inlet valve FSR-IV and VSR-IV.

V. DISCUSSION

In Table 5, the main results from Section IV are listed in a summarizing table. For each result, the absolute value V is given for the 3 DOF topology VSR-IV. For the other toplogies the relative differences δV compared with toplogy VSR-IV are listed, which are calculated as follows:

$$\delta V_{\text{xxx-xxx}} = \frac{V_{\text{xxx-xxx}} - V_{\text{VSR-IV}}}{V_{\text{VSR-IV}}} \tag{24}$$

To quantify the operating range, it is defined as the surface area of the contour plots in Section IV-A. To highlight the results, a color code is used, where green is used to highlight minor relative losses and yellow and red are used for medium and major relative differences, respectively.

From the results, it is clear that adding the inlet valve as a DOF significantly increases the operating ranges towards higher possible fallheads in turbine mode and higher powers in pump mode. In addition, the efficiency is also increased. Next, the impact of using variable speed ratio control on the operating range depends on whether inlet valve control is also used. Comparing topology VSR-NIV to topology FSR-NIV, next to an increase in efficiency in both pump and turbine mode, the operating range is significantly increased. However, the increase in operating range and efficiency is not as high when comparing topologies VSR-IV and FSR-IV. Furthermore, in the high efficiency zones (towards the operating range limit), the efficiency difference is only $< 1\%$, with larger efficiency differences occurring only at subnominal operating points in pump mode, reflecting in a relative decrease in average efficiency of 4.9%.

From the cycle scenarios, it can be concluded that using only the first runner's rotational speed as a DOF (topology FSR-NIV), the significantly reduced operating range (−44.9% and −53.4% for turbine and pump mode, respectively) results in this topology having the lowest energy storage capacity for all cycles (−30.4% and 30.0% for the optimal cycle and FCR cycle, respectively). Next, using a variable speed ratio and no inlet valve (topology VSR-NIV), the same energy storage capacity can be reached as topology VSR-IV in the FCR scenarios, but at a relative cycle efficiency reduction 8.9%. In the optimal efficiency cycle, topology VSR-NIV reaches a round-trip efficiency which is relatively 7.1% lower than in topology VSR-IV, at a storage capacity reduction of 10.6%. Due to the reduced operating range at subnominal operating points, the energy storage capacity in the FRR scenario is reduced by 82.6% compared with topology VSR-IV. The results indicate that a topology without the inlet valve as a DOF is not optimal for the optimal efficiency and FCR cycles, and unsuitable for FRR services. Using the topology with all three DOFs (VSR-IV), the efficiency and energy storage capacity are always maximal. However, the magnitude of the difference with topology FSR-IV (fixed speed ratio, variable inlet valve) differs for the different cycle scenarios. For the optimal efficiency cycle, the efficiency difference between topologies VSR-IV and FSR-IV is only 0.6%, with a relative energy storage capacity deficit of 10.6% for topology FSR-IV. However, for operating scenarios providing grid services, the added benefit of using all three degrees of freedom becomes significant. In the FCR scenario, the cycle efficiency difference increases to 3.2% at an energy capacity decrease of 16.0%. In the FRR scenario, the cycle efficiency difference becomes 15.1%, with a 10.6% decrease in the energy storage capacity.

For a full cycle along the total fallhead range with variable power, an energy storage capacity of 58.6 Wh/m^2 with a round-trip efficiency of 67.5% can be reached by using all three DOFs. This efficiency is lower than that of electrochemical batteries (70%-90%), but higher than that of hydrogen storage (20%-66%). Next, this PHS system is slightly less efficient than high-head PHS systems (70%-85%), which is due to the higher flow rate-to-power ratio in this low-head system, resulting in higher conduit losses. However, due to the higher lifetime and lower cost, it can be concluded that a PHS system comprising a CR RPT has significant potential to compete with new battery and hydrogen storage facilities for countries with a flat topography.

TABLE 5. Overview of the main results from Section IV, with the absolute value given for topology VSR-IV and the relative difference compared with topology VSR-IV for the other topologies.

	FSR NIV	VSR NIV	FSR IV	VSR IV
	Relative difference δV			Value V
Turbine				
Max. efficiency	-0.6%	0.0%	-0.6%	82.9%
Average efficiency	-3.5%	-3.1%	-0.9%	62.1%
Operating range	-44.9%	-38.1%	-1.7%	44 MW·m
Pump				
Max. efficiency	-1.0%	0.0%	-1.0%	84.1%
Average efficiency	-0.7%	0.0%	-4.9%	70.7%
Operating range	-53.4%	-37.5%	-5.3%	52 MW·m
Optimal cycle				
Cycle efficiency	-5.2%	-7.1%	-0.6%	67.5%
Energy capacity	-30.4%	-10.6%	-10.6%	58.6 Wh/m^2
FCR cycle				
Cycle efficiency	-5.4%	-8.9%	-3.2%	63.3%
Energy capacity	-30.0%	0.0%	-16.0%	32.6 Wh/m^2
FRR cycle				
Cycle efficiency	-	-18.2%	-15.1%	19.2%
Energy capacity	-	-82.6%	-10.6%	58.6 Wh/m^2

VI. CONCLUSION

In this paper, the impact of dual variable speed and inlet valve control on the efficiency of a novel contra-rotating RPT for low-head PHS is investigated. To analyze the full system efficiency, a hydraulic model is used that utilizes

CFD simulations and includes the conduit major, minor, and variable valve losses. For the electric machines, PMSMs are used and are modeled in the *dq* reference frame, where both the copper and iron losses are represented, with the latter including the eddy current and speed-dependent hysteresis losses. Next, the conduction and switching losses of commercially available medium voltage VFDs are replicated using IGBT data and simulated switching times. For every combination of the degrees of freedom, an efficiency map is simulated that reflects the maximum efficiency and operating range that can be reached using the available DOFs.

It is found that, using both inlet valve control and variable speed control, both the operating range and efficiency are maximal. In a variable power cycle between the fallhead limits using all three DOFs, a hydraulic energy storage capacity of 58.6 Wh per unit of reservoir area can be achieved at a round-trip efficiency of 67.5%, which allows this technology to compete with other storage technologies in regions without suitable topography for high-head PHS. Eliminating the inlet valve as a DOF has the highest influence on the operating range (with relative decreases of $> 37.5\%$), while also having a relative $>$ 3.1% average efficiency reduction in turbine mode. It is concluded that a topology with a fixed speed ratio and no variable inlet valve is not viable, bearing a relative $>$ 44.9% reduction in operating range and a $> 3.5\%$ average efficiency reduction compared with the 3 DOF topology. In a topology with inlet valve control, the benefits of adding variable speed ratio control as a third degree of freedom are not as significant in an optimal efficiency cycle, with a relative cycle efficiency difference of only 0.6% and a relative energy storage capacity difference of 10.6%. However, in frequency reserve scenarios, the relative cycle efficiency difference significantly increases to 3.2% and 15.1% for the FCR and FRR scenarios, respectively, with energy capacity differences of 16.0% and 10.6%. Therefore, it can be concluded that using both variable speed ratio and inlet valve control, a significant increase in performance is found, which becomes more apparent when providing frequency services.

The outcomes of this study demonstrate the technical feasibility of low-head pumped hydropower storage and the importance of utilizing the available degrees of freedom to optimize the efficiency and operating range. However, several key avenues can be explored in future work. The authors propose to extend the steady-state model to a dynamic model that captures the transients in the RPT, conduit, electric machines, and power electronics in order to develop a control architecture that exploits the available degrees of freedom to reach power setpoints at optimal efficiency. Furthermore, the authors highlight the importance of analyzing the impact of providing frequency reserves on the reliability of the proposed hydropower storage system. Although these effects have been described in literature for medium and high head systems [34], [35], [36], the increased flow rate in this low-head system affects the dynamic loads on the RPT and conduit, e.g., water hammer effect. Additionally, these insights can be used to identify critical components to model and monitor for predictive maintenance, as effective maintenance procedures and minimization of downtime is imperative for an off-shore storage system [37], [38]. Finally, an economical analysis on the capital costs and the balance between the increased revenue with frequency reserves and increased cost of operation and maintenance, caused by providing these reserves, can lead to the optimal design and operation of this low-head PHS system.

ACKNOWLEDGMENT

This research is perfomed in context of the EU H2020 ALPHEUS project. The CFD computations were enabled by resources provided by the National Academic Infrastructure for Supercomputing in Sweden (NAISS) and the Swedisch National Infrastructure for Computing (SNIC) at NSC and C3SE.

REFERENCES

[1] International Energy Agency. (Jan. 2023). *Energy Technology Perspectives 2023*. [Online]. Available: https://www.iea.org/reports/energy-technology-perspectives-2023

[2] International Energy Agency. (Dec. 2022). *Renewables 2022*. [Online]. Available: https://www.iea.org/reports/renewables-2022

[3] V. Jülch, "Comparison of electricity storage options using levelized cost of storage (LCOS) method," *Appl. Energy*, vol. 183, pp. 1594–1606, Dec. 2016, doi: 10.1016/j.apenergy.2016.08.165.

[4] REN21. (2022). *Renewables 2022, Global Status Report*. [Online]. Available: https://www.ren21.net/wp-content/uploads/2019/05/GSR2022_Full_Report.pdf

[5] J. Mitali, S. Dhinakaran, and A. A. Mohamad, "Energy storage systems: A review," *Energy Storage Saving*, vol. 1, no. 3, pp. 166–216, Sep. 2022, doi: 10.1016/j.enss.2022.07.002.

[6] E. Agneholm and E. A. Jansson. (May 2017). *FCP Project Summary Report*. European Network of Transmission System Operators for Electricity. [Online]. Available: https://www.svk.se/contentassets/e5a38b7a16a443b290f5d49d42ea03c0/1—fcp-project-summary-report.pdf

[7] T. Mercier, J. Jomaux, E. De Jaeger, and M. Olivier, "Provision of primary frequency control with variable-speed pumped-storage hydropower," in *Proc. IEEE Manchester PowerTech*, Manchester, U.K., Sep. 2017, pp. 1–6, doi: 10.1109/PTC.2017.7980920.

[8] J. P. Hoffstaedt, D. P. K. Truijen, J. Fahlbeck, L. H. A. Gans, M. Qudaih, A. J. Laguna, J. D. M. De Kooning, K. Stockman, H. Nilsson, P.-T. Storli, B. Engel, M. Marence, and J. D. Bricker, "Low-head pumped hydro storage: A review of applicable technologies for design, grid integration, control and modelling," *Renew. Sustain. Energy Rev.*, vol. 158, Apr. 2022, Art. no. 112119, doi: 10.1016/j.rser.2022.112119.

[9] E. B. Prasasti, M. Aouad, M. Joseph, M. Zangeneh, and K. Terheiden, "Optimization of pumped hydro energy storage design and operation for offshore low-head application and grid stabilization," *Renew. Sustain. Energy Rev.*, vol. 191, Mar. 2024, Art. no. 114122, doi: 10.1016/j.rser.2023.114122.

[10] R. A. Ruiz, L. H. de Vilder, E. B. Prasasti, M. Aouad, A. De Luca, B. Geisseler, K. Terheiden, S. Scanu, A. Miccoli, V. Roeber, M. Marence, R. Moll, J. D. Bricker, and N. Goseberg, "Low-head pumped hydro storage: A review on civil structure designs, legal and environmental aspects to make its realization feasible in seawater," *Renew. Sustain. Energy Rev.*, vol. 160, May 2022, Art. no. 112281, doi: 10.1016/j.rser.2022.112281.

[11] M. Simão and H. Ramos, "Hybrid pumped hydro storage energy solutions towards wind and PV integration: Improvement on flexibility, reliability and energy costs," *Water*, vol. 12, no. 9, p. 2457, Sep. 2020, doi: 10.3390/w12092457.

[12] R. GhoshThakur, S. Balachandran, and S. GonChaudhuri, "Analysis of multimodal performance of a hybrid solar pumped storage system for enhanced energy security in rural areas," *Int. J. Green Energy*, vol. 1, pp. 1–19, Oct. 2023, doi: 10.1080/15435075.2023.2264414.

[13] M. Mueller, J. Pander, and J. Geist, "Evaluation of external fish injury caused by hydropower plants based on a novel field-based protocol," *Fisheries Manage. Ecol.*, vol. 24, no. 3, pp. 240–255, May 2017, doi: 10.1111/fme.12229.

[14] A. Miccoli, A. De Luca, J. Bricker, F. T. Vriese, R. Moll, and G. Scapigliati, "Stress response to entrainment flow speed near pump inlet fish screens in two model teleost species, anguilla anguilla and oncorhynchus mykiss," *Fishes*, vol. 8, no. 3, p. 139, Feb. 2023, doi: 10.3390/fishes8030139.

[15] J. Fahlbeck, H. Nilsson, S. Salehi, M. Zangeneh, and M. Joseph, "Numerical analysis of an initial design of a counter-rotating pump-turbine," *IOP Conf. Ser., Earth Environ. Sci.*, vol. 774, no. 1, Jun. 2021, Art. no. 012066, doi: 10.1088/1755-1315/774/1/012066.

[16] J.-H. Kim, B.-M. Cho, S. Kim, J.-W. Kim, J.-W. Suh, Y.-S. Choi, T. Kanemoto, and J.-H. Kim, "Design technique to improve the energy efficiency of a counter-rotating type pump-turbine," *Renew. Energy*, vol. 101, pp. 647–659, Feb. 2017, doi: 10.1016/j.renene.2016.09.026.

[17] G. Olimstad, T. Nielsen, and B. Børresen, "Stability limits of reversible-pump turbines in turbine mode of operation and measurements of unstable characteristics," *J. Fluids Eng.*, vol. 134, no. 11, Nov. 2012, Art. no. 111202, doi: 10.1115/1.4007589.

[18] I. Iliev, C. Trivedi, E. Agnalt, and O. G. Dahlhaug, "Variable-speed operation and pressure pulsations in a Francis turbine and a pump-turbine," *IOP Conf. Ser., Earth Environ. Sci.*, vol. 240, Mar. 2019, Art. no. 072034, doi: 10.1088/1755-1315/240/7/072034.

[19] A. Morabito and P. Hendrick, "Pump as turbine applied to micro energy storage and smart water grids: A case study," *Appl. Energy*, vol. 241, pp. 567–579, May 2019, doi: 10.1016/j.apenergy.2019.03.018.

[20] A. Morabito, G. de Oliveira e Silva, and P. Hendrick, "Deriaz pump-turbine for pumped hydro energy storage and micro applications," *J. Energy Storage*, vol. 24, Aug. 2019, Art. no. 100788, doi: 10.1016/j.est.2019.100788.

[21] D. Biner, V. Hasmatuchi, D. Violante, S. Richard, S. Chevailler, L. Andolfatto, F. Avellan, and C. Münch, "Engineering & performance of DuoTurbo: Microturbine with counter-rotating runners," *IOP Conf. Ser., Earth Environ. Sci.*, vol. 49, Nov. 2016, Art. no. 102013, doi: 10.1088/1755-1315/49/10/102013.

[22] D. Biner, V. Hasmatuchi, L. Rapillard, S. Chevailler, F. Avellan, and C. Münch-Alligné, "DuoTurbo: Implementation of a counter-rotating hydroturbine for energy recovery in drinking water networks," *Sustainability*, vol. 13, no. 19, p. 10717, Sep. 2021, doi: 10.3390/su131910717.

[23] J. Fahlbeck, H. Nilsson, and S. Salehi, "Surrogate based optimisation of a pump mode startup sequence for a contra-rotating pump-turbine using a genetic algorithm and computational fluid dynamics," *J. Energy Storage*, vol. 62, Jun. 2023, Art. no. 106902, doi: 10.1016/j.est.2023.106902.

[24] J. D. M. De Kooning, T. L. Vandoorn, J. Van De Vyver, B. Meersman, and L. Vandevelde, "Displacement of the maximum power point caused by losses in wind turbine systems," *Renew. Energy*, vol. 85, pp. 273–280, Jan. 2016, doi: 10.1016/j.renene.2015.06.052.

[25] D. P. K. Truijen, J. D. M. De Kooning, D. Fauconnier, H. Vansompel, P. Sergeant, and K. Stockman, "Axial flux PMSM power take-off for a rim-driven contra-rotating pump-turbine," in *Proc. IEEE PES 14th Asia–Pacific Power Energy Eng. Conf. (APPEEC)*, Melbourne, VIC, Australia, Nov. 2022, pp. 1–6, doi: 10.1109/APPEEC53445.2022.10072056.

[26] J.-W. Chin, K.-S. Cha, M.-R. Park, S.-H. Park, E.-C. Lee, and M.-S. Lim, "High efficiency PMSM with high slot fill factor coil for heavy-duty EV traction considering AC resistance," *IEEE Trans. Energy Convers.*, vol. 36, no. 2, pp. 883–894, Jun. 2021, doi: 10.1109/TEC.2020.3035165.

[27] H. Vansompel, P. Sergeant, and L. Dupré, "Optimized design considering the mass influence of an axial flux permanent-magnet synchronous generator with concentrated pole windings," *IEEE Trans. Magn.*, vol. 46, no. 12, pp. 4101–4107, Aug. 2010, doi: 10.1109/TMAG.2010.2070075.

[28] TMEIC Corp. (Jul. 2019). *Fact Sheet VACON 3000 Enclosed Drive*. [Online]. Available: https://files.danfoss.comdownload/Drives/DKDDPFP907A302_VACON_3000_Enclosed_Drive_LR.pdf

[29] Danfoss Drives. (2021). *TMdrive-50 Medium Voltage 3-Level IGBT System Drive*. [Online]. Available: https://www.tmeic.com/sites/default/files/assets/files/library/D-0004%20TMdrive-50.pdf

[30] (Oct. 2020). *HiPak IGBT Module 5SNA 1200E330100*. ABB Power Grids Switzerland Ltd, Semiconductors, Frabrikstrasse 3, CH-5600 Lenzburg, Switzerland, Frabrikstrasse 3, CH-5600 Lenzburg, Switzerland. [Online]. Available: https://search.abb.com/library/Download.aspx?DocumentID=5SYA1556-05&LanguageCode=en&DocumentPartId=&Action=Launch

[31] M. Ikonen, O. Laakkonen, and M. Kettunen. (Jan. 2005). *Two-level and Three-level Converter Comparison in Wind Power Application*. [Online]. Available: https://www.researchgate.net/publication/228784889_Two-Level _ and _ Three - Level _ Converter _ Comparison _ in _ Wind _ Power _Application

[32] E. Hart, W. E. Leithead, and J. Feuchtwang, "Wind turbine c p,max and drivetrain-losses estimation using Gaussian process machine learning," *J. Phys., Conf. Ser.*, vol. 1037, Jun. 2018, Art. no. 032024, doi: 10.1088/1742-6596/1037/3/032024.

[33] TransnetBW. (2022). *Ancillary Services: Control Reserve Demand + Activation*. Accessed: Sep. 8, 2023. [Online]. Available: https://www.transnetbw.de/en/energy-market/ancillary-services/control-reserve-demand-activation

[34] L. Saarinen, P. Norrlund, W. Yang, and U. Lundin, "Allocation of frequency control reserves and its impact on wear and tear on a hydropower fleet," *IEEE Trans. Power Syst.*, vol. 33, no. 1, pp. 430–439, Jan. 2018, doi: 10.1109/TPWRS.2017.2702280.

[35] S. Cassano and F. Sossan, "Stress-informed control of medium- and high-head hydropower plants to reduce penstock fatigue," *Sustain. Energy, Grids Netw.*, vol. 31, Sep. 2022, Art. no. 100688, doi: 10.1016/j.segan.2022.100688.

[36] B. A. Bhatti, S. Hanif, J. Alam, B. Mitra, R. Kini, and D. Wu, "Using energy storage systems to extend the life of hydropower plants," *Appl. Energy*, vol. 337, May 2023, Art. no. 120894, doi: 10.1016/j.apenergy.2023.120894.

[37] A. Betti, E. Crisostomi, G. Paolinelli, A. Piazzi, F. Ruffini, and M. Tucci, "Condition monitoring and predictive maintenance methodologies for hydropower plants equipment," *Renew. Energy*, vol. 171, pp. 246–253, Jun. 2021, doi: 10.1016/j.renene.2021.02.102.

[38] E. Georgievskaia, "Predictive analytics as a way to smart maintenance of hydraulic turbines," *Procedia Structural Integrity*, vol. 28, pp. 836–842, Jun. 2020, doi: 10.1016/j.prostr.2020.10.098.

DAAN P. K. TRUIJEN (Graduate Student Member, IEEE) was born in Antwerpen, Belgium, in 1997. He received the Master of Science degree in electrical engineering technology from Ghent University, Belgium, in 2020. He joined the Department of Electromechanical, Systems and Metal Engineering, Faculty of Engineering and Architecture, Ghent University, as a Doctoral Researcher, in 2020. His current research interests include the development of drivetrains and control architectures for novel PHS systems. He is a member of the Dynamical Systems and Control (DySC) Research Group and the FlandersMake@UGent MIRO Core Laboratory.

JUSTUS P. HOFFSTAEDT was born in Duesseldorf, Germany, in 1994. He received the Master of Science degree in sustainable energy systems from The University of Edinburgh, U.K., in 2019. He is currently pursuing the Ph.D. degree with the Department of Maritime and Transport Technology, Faculty of Mechanical, Maritime and Materials Engineering, Delft University of Technology, The Netherlands. Previously, he worked for the NGO Comet-ME on the provision of off-grid water and renewable energy systems in Palestine. His research interests include physical modeling and experimental validation of hydromechanical energy storage systems.

JONATHAN FAHLBECK was born in Linköping, Sweden, in 1992. He received the Master of Science degree in mechanical engineering from the Chalmers University of Technology, Sweden, in 2018, where he is currently pursuing the Ph.D. degree with the Department of Mechanics and Maritime Sciences, Division of Fluid Dynamics. From 2018 to 2020, he was a CFD Engineering Consultant with SEMCON AB, Sweden. His research interests include the numerical modeling of the flow field in hydro pump turbines using CFD, with a particular interest in transients.

ANTONIO JARQUIN LAGUNA was born in Toluca, Mexico, in 1984. He received the B.Eng. degree in mechanical engineering from the National University of Mexico (UNAM), in 2007, and the Master of Science and Ph.D. degrees in offshore wind energy from Delft University of Technology, in 2010 and 2017, respectively. Since 2019, he has been an Assistant Professor with the Department of Maritime and Transport Technology, Faculty of Mechanical, Maritime and Materials Engineering, Delft University of Technology, The Netherlands. He conducted research on fluid-power applications for wind energy systems and worked as an Innovation Engineer on the design of floating tidal energy systems for the offshore company Bluewater Energy Services. His current research interests include physical modeling of offshore renewable energy technologies and marine energy systems.

HÅKAN NILSSON was born in Falkenberg, Sweden, in 1971. He received the Master of Science degree in physical oceanography from Gothenburg University, in 1997, and the Ph.D. degree in thermo and fluid dynamics from the Chalmers University of Technology, Gothenburg, Sweden, in 2002. Since 2015, he has been a Full Professor with the Department of Mechanics and Maritime Sciences, Division of Fluid Dynamics, Chalmers University of Technology. From 2018 to 2019, he was a Visiting Professor with TU Delft, The Netherlands. His research interests include computational, experimental, and analytical fluid dynamics, involving method development, studies of particular applications, and validation. The main application area is hydropower, including swirling flow in turbines and heat transfer in electric generators, turbulence modeling, rotor-stator interaction, rotor dynamics, cavitation modeling, and system coupling. He is a member of the International Association for Hydro-Environment Engineering and Research (IAHR) and the Head of the OpenFOAM Turbomachinery Special Interest Group.

KURT STOCKMAN was born in Kortrijk, Belgium, in 1972. He received the master's degree in industrial engineering (electrotechnics) from PIH Kortrijk, in 1994, and the Ph.D. degree from KU Leuven, in 2003. He is currently a Full Professor with the Department of Electromechanical, Systems and Metal Engineering, Faculty of Engineering and Architecture, Ghent University, Belgium. His research interests include the design, control, and energy efficiency of electromechanical drivetrains and mechatronic systems both in the industrial context, automotive, and renewable energy applications. A state-of-the-art laboratory is used for the validation of the electromechanical drivetrains research results and for characterization testing services for industry. He has a long tradition in collaboration with industry. He is a partner of FlandersMake@UGent, Flanders, Belgium, the strategic research center for the manufacturing industry. Within FlandersMake, he is active in the motion products cluster. He is an Active Member of the IEC Level and a member of the Dynamical Systems and Control (DySC) Research Group.

JEROEN D. M. DE KOONING (Senior Member, IEEE) was born in Kapellen, Belgium, in 1987. He received the Master of Science and Ph.D. degrees in electromechanical engineering from Ghent University, Belgium, in 2010 and 2015 respectively. Since 2019, he has bee an Assistant Professor with the Department of Electromechanical, Systems and Metal Engineering, Faculty of Engineering and Architecture, Ghent University, Belgium. In 2022, he was a Visiting Professor with the Lappeenranta University of Technology, Finland. He conducted research on current waveform shaping techniques for permanent magnet synchronous machines and optimal control and design of renewable energy systems. His research interests include modeling, optimization and control of mechatronic systems, drivetrains, and manufacturing machines in an industry 4.0 context, with a particular interest in digital twins. He is a member of the Dynamical Systems and Control (DySC) Research Group and the FlandersMake@UGent MIRO Core Laboratory.